Received: 23 May 2024 | Revised: 20 September 2024 | Accepted: 20 October 2024

DOI: 10.1002/eom2.12501

RESEARCH ARTICLE

EcoMat FUNCTIONAL MATERIALS FOR GREEN ENERGY AND ENVIRONMENT WILEY

A universal reverse-cool annealing strategy makes two-dimensional Ruddlesden-popper perovskite solar cells stable and highly efficient with V_{oc} exceeding 1.2 V

Zhongqi Xie[1] | **Huiming Luo**[2] | **Qing-Song Jiang**[1] | **Ya Zhao**[1] | **Yong Peng**[3] | **Ligang Yuan**[4] | **Keyou Yan**[4] | **Mojtaba Abdi-Jalebi**[2]

[1]Faculty of electronic information engineering, Huaiyin Institute of Technology, Huai'an, China

[2]Institute for Materials Discovery, University College London, London, UK

[3]State Key Lab of Advanced Technology for Materials Synthesis and Processing, Wuhan University of Technology, Wuhan, China

[4]School of Environment and Energy, State Key Laboratory of Luminescent Materials and Devices, Guangdong Provincial Key Laboratory of Solid Wastes Pollution Control and Recycling, South China University of Technology, Guangzhou, China

Correspondence

Qing-Song Jiang, Faculty of electronic information engineering, Huaiyin Institute of Technology, Huai'an 223003, China.
Email: jiangqingsong05@hyit.edu.cn

Yong Peng, State Key Lab of Advanced Technology for Materials Synthesis and Processing, Wuhan University of Technology, Wuhan 430070, China.
Email: yongpeng@whut.edu.cn

Mojtaba Abdi-Jalebi, Institute for Materials Discovery, University College London, Malet Place, London, WC1E 7JE, UK.
Email: m.jalebi@ucl.ac.uk

Funding information

National Natural Science Foundation of China, Grant/Award Number: 61804062; The open research fund of State Key Laboratory of Advanced Technology for Materials Synthesis and Processing (Wuhan University of Technology), Grant/Award Number: 2023-KF-21; The open research fund of State Key Laboratory of Organic Electronics and Information Displays, Grant/Award Number: SKL2023004; Department for Energy Security and Net Zero,

Abstract

Two-dimensional Ruddlesden-Popper (2D RP) layered metal-halide perovskites have garnered increasing attention due to their favorable optoelectronic properties and enhanced stability in comparison to their three-dimensional counterparts. Nevertheless, precise control over the crystal orientation of 2D RP perovskite films remains challenging, primarily due to the intricacies associated with the solvent evaporation process. In this study, we introduce a novel approach known as reverse-cool annealing (RCA) for the fabrication of 2D RP perovskite films. This method involves a sequential annealing process at high and low temperatures for wet perovskite films. The resulting RCA-based perovskite films show the smallest root-mean-square value of 23.1 nm, indicating a minimal surface roughness and a notably compact and smooth surface morphology. The low defect density in these 2D RP perovskite films with exceptional crystallinity suppresses non-radiative recombination, leading to a minimal non-radiative open-circuit voltage loss of 149 mV. Moreover, the average charge lifetime in these films is extended to 56.3 ns, thanks to their preferential growth along the out-of-plane direction. Consequently, the leading 2D RP perovskite solar cell achieves an impressive power conversion efficiency of 17.8% and an open-circuit voltage of 1.21 V. Additionally, the stability of the 2D RP perovskite solar cell, even without encapsulation, exhibits substantial improvement, retaining 97.4% of its initial efficiency after 1000 hours under a

Zhongqi Xie and Huiming Luo contributed equally to this study.

Grant/Award Number: NEXTCCUS (691712); ACT programme (Accelerating CCS Technologies, Horizon2020 Project No. 691712), Grant/Award Number: 327327

nitrogen environment. The RCA strategy presents a promising avenue for advancing the commercial prospects of 2D RP perovskite solar cells.

KEYWORDS

crystal orientation, open-circuit voltage, perovskite solar cells, reverse-cool annealing strategy, Ruddlesden-popper

1 | INTRODUCTION

Perovskite solar cells (PSCs) have received much attention because of their high absorption coefficient, large charge carrier mobility, and excellent photovoltaic performance.[1,2] At present, through diligent optimization of fabrication protocols, the maximal power conversion efficiency (PCE) of PSCs has experienced a precipitous increase, attaining values exceeding 26%.[3,4] Except for the PCE, operational stability is another key parameter that needs consideration toward commercialization.[5–7] It is interestingly found that two-dimensional Ruddlesden-Popper (2D RP) PSCs display long-term environmental stability by introducing bulky large cations (e.g., phenylethylammonium (PEA), 4-fluorophenylethylammonium (4FPEA)).[8,9] However, carrier transport ability is suppressed due to the quantum confinement effect and random crystal orientation of 2D RP perovskite films.[10] Thus, the photovoltaic performance of 2D RP PSCs is still lower than that of their 3D counterparts.[11]

Various strategies are proposed to fabricate highly efficient and stable 2D PSCs, including solvent engineering, additive engineering, and cation engineering.[12–16] Zhu and co-workers adjusted the content of dimethyl sulfoxide (DMSO) in precursors to tune the quality of obtained 2D RP perovskite $(PEA)_2(MA)_4Pb_5I_{16}$.[12] Additives like Lewis acids and Lewis bases were employed to assist the crystallization of 2D RP perovskite films and induce the out-of-plane direction.[17,18] For example, ammonium thiocyanate (NH_4SCN) was employed as an additive to control crystallographic orientation of 2D RP perovskite films, leading to high-efficiency charge transport.[18] Besides, the bulky large cations were also explored to improve the PCE of 2D RP PSCs by tuning their crystal structure.[19] Shao and colleagues have illustrated this concept by substituting phenylethylammonium (PEA) with 4-fluorophenethylammonium (4FPEA), resulting in an impressive increase in PCE of 2D RP PSCs, from 11.1% to 17.3%.[8] The enhancement of PCE is attributed to the fast charge dissociation and preferentially grown along the out-of-plane direction by inducing the fluorinated PEA cation. Meanwhile, the environmental stability of PSCs is also improved owing to the hydrophobic property of fluorinated cation.[8] Although those strategies can improve PCE and stability of 2D RP PSCs, the complexity and uncontrollability of 2D RP perovskite films still need further exploration.

The quality of 2D RP perovskite films is in correlation with the photovoltaic performance of PSCs. As the evaporation rate of solvents, nucleation and growth rate of grains are highly dependent on annealing processes of 2D RP perovskite films. Therefore, the annealing strategy is very important process to promote the ordered distribution of multiple phases along the out-of-plane direction. For example, a hot-casting strategy was used to fabricate the uniform 2D RP perovskite films with excellent crystallinity, providing the more charge-transport channels.[20,21] 2D RP perovskite $(4FPEA)_2(FA_{0.3}MA_{0.7})_4Pb_5I_{16}$ ($n = 5$) was fabricated by a hot-casting strategy (e.g., the substrate heated to 100 °C) and exhibited a preferential vertical orientation.[11] However, the repeatability of 2D RP PSCs obtained from a hot-casting strategy needs to be further optimized, due to the quality of 2D RP perovskite films being deeply reliant on substrate temperature.[22] Additionally, several annealing strategies, such as close-space annealing and two-second-annealed methods, are still explored for the fabrication of perovskite films in detail.[23,24] Interestingly, a nonisothermal strategy was also used to fabricate high-quality perovskite films through illuminating wet film by a NIR lamp with temperature more than 100 °C.[25] The perovskite films with high phase stability, small surface lattice space, and high bonding energy were also fabricated by an air-processed thermal-shocking strategy with high temperature above 180 °C.[26] From the above discussion, the flash crystallization process with high nucleation and growth rate has been obtained by the flash-annealing approach, which is beneficial to fabricating high-quality perovskite films. Therefore, it is highly desirable to develop a novel flash-annealing approach to fabricate 2D RP PSCs.

In this work, 2D RP perovskite $(4FPEA)_2(MA_{0.9}FA_{0.1})_3Pb_4I_{13}$ films are fabricated by reverse-cool annealing (RCA) strategy. The first step accelerated the nucleation and growth of 2D RP perovskite films by annealing at 120 °C for 8 s. The second step is strengthening the crystal quality by annealing at 80 °C for 5 min. Additionally, 2D RP PSCs preferentially grow along the

vertical direction. The results demonstrate that 2D RP perovskite films display high crystallinity, long charge lifetime, and strong carrier transport ability. As a result, the 2D RP PSC with RCA shows a significant PCE of 17.8%, which is higher than those of the 2D RP PSCs with high-temperature annealing (HTA) (7.8%) and low-temperature annealing (LTA) (12.7%).

2 | RESULTS AND DISCUSSION

Two-dimensional Ruddlesden-Popper perovskite (4FPEA)$_2$(MA$_{0.9}$FA$_{0.1}$)$_3$Pb$_4$I$_{13}$ films are fabricated by three different annealing strategies, including LTA, HTA, and RCA. Figure 1A shows the fabrication process of perovskite films based on LTA, HTA, and RCA. In the LTA

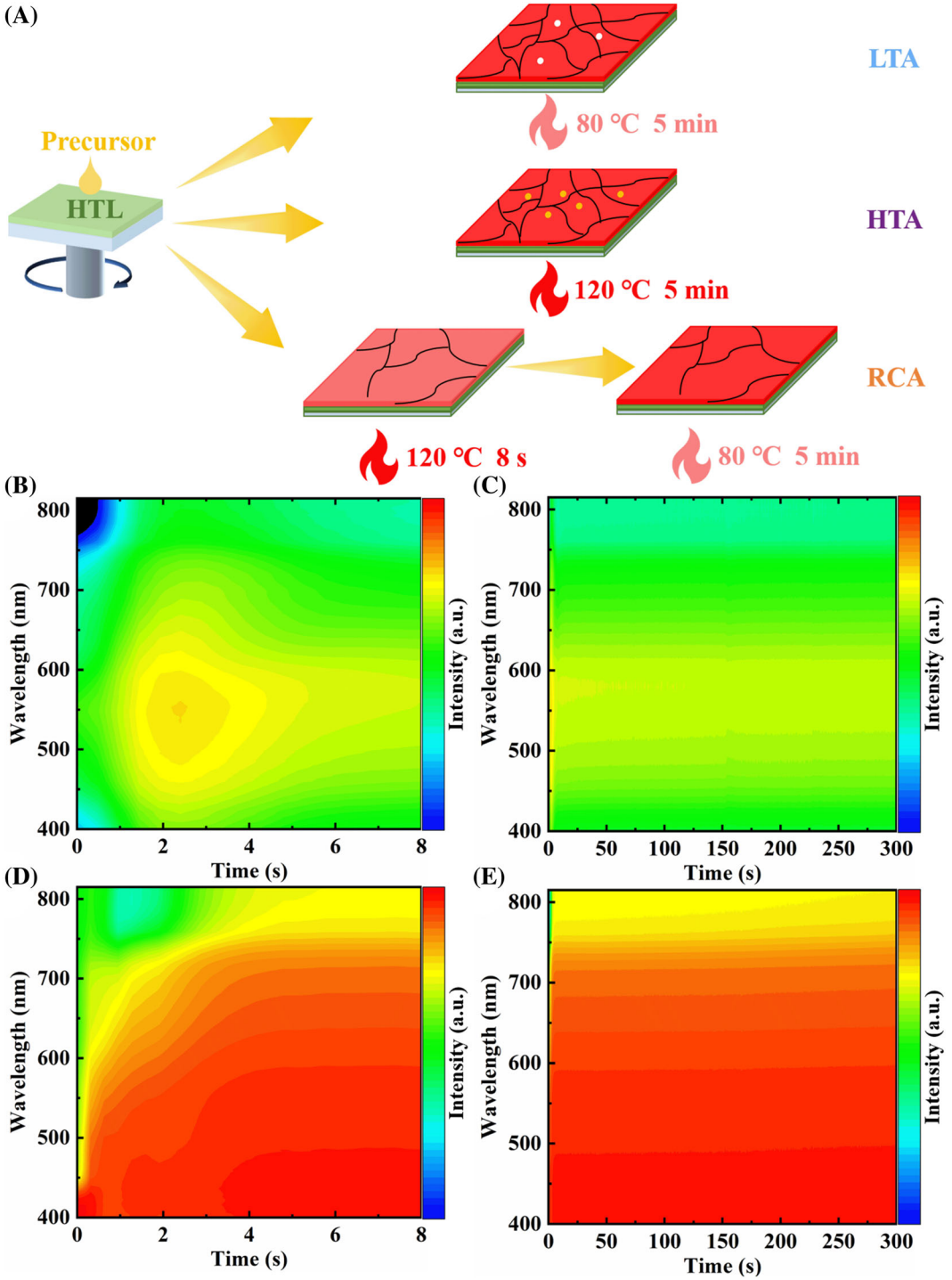

FIGURE 1 (A) The schematic of the fabrication process of perovskite films with LTA, HTA, and RCA. In situ absorption evolution during the annealing process for the perovskite films with LTA for 8 s (B) and 300 s (C), HTA for 8 s (D) and 300 s (E).

strategy, the wet perovskite films are heated at 80 °C for 5 min, resulting in as-prepared perovskite films with some pinholes. The in situ absorption evolution during the annealing process for the perovskite film based on LTA are shown in Figure 1B,C. The absorption spectrum red-shifts after placing the wet perovskite film on a hot platform at 80 °C. However, the weak absorption intensity of the absorption spectrum indicates the formation of perovskite crystallites.[21] For the HTA strategy, a temperature as high as 120 °C is used to obtain perovskite films. It is observed that high annealing temperature (e.g., 120 °C) damage the crystal quality of the obtained perovskite films by exposing PbI_2 crystal grains. From Figure 1D,E, the crystallization reaction is triggered by the high temperature of 120 °C in 1 s after placing the wet perovskite film on a hot platform. After approximately 6–8 s, the absorption spectrum of the perovskite films rapidly red-shifts, signifying the formation of the perovskite film. And then the absorption spectrum eventually exhibits a continuous profile. Therefore, the optimized time of high temperature annealing process is around 8 s. Regarding the effects of annealing time for both LTA and HTA, the photovoltaic parameters are displayed in Table S1. The RCA strategy, on the other hand, effectively improves the crystal quality of the perovskite films. In this approach, the wet perovskite films are heated at 120 °C for 8 s to achieve a high nucleation and growth rate during the first step, which promotes crystal growth along the out-of-plane direction, as shown in Figure S1a. Subsequently, the low-temperature annealing step (80 °C for 5 min) in the second stage further facilitates the formation of the uniform and smooth perovskite films. To clarify the effect of the low-temperature annealing step, the perovskite film with annealing at 120 °C for 8 s (marked as HTA-8) is characterized by the steady-state photoluminescence (PL) spectra, as shown in Figure S1b. The PL intensity of perovskite film with RCA is larger than that of the perovskite film with HTA-8, demonstrating the improvement the perovskite crystallization quality through low-temperature annealing step. Furthermore, the corresponding perovskite films are used to fabricate PSCs. Figure S2 shows *J-V* curves of the PSCs based on RCA and HTA-8. The photovoltaic performance of the PSC with RCA is higher than that of the PSC with HTA-8 with the detailed data in Table S2.

To verify the aforementioned hypothesis, the morphologies of perovskite films were characterized by scanning electron microscope (SEM) and atom force microscope (AFM). Figure 2A–C shows plane-view SEM images of perovskite films produced through LTA, HTA, and RCA. From Figure 2A and Figure S3, the RCA-based perovskite film exhibits a notably compact and smooth surface. As can be seen in Figure 2B, a deleterious impact on the surface of the HTA-derived perovskite film is apparent. The white regions denote the presence of PbI_2 crystal grains, resulting from the decomposition of perovskite films.[27] In contrast, as depicted in Figure 2C, it is evident that the LTA-derived perovskite film displays conspicuous pinholes and grain boundaries. Figure 2D shows the cross-sectional SEM image of the RCA-derived perovskite film. Interestingly, continuous large grains with almost no grain boundary are obviously observed for the RCA-derived perovskite film. The thickness of the RCA-derived perovskite film is approximately 440 nm. The strong smooth surface and vertical-orientation of the RCA-derived perovskite film is beneficial for improving the charge transport and extraction ability, resulting in the dramatic improvement of short-circuit current density (J_{sc}). From Figure 2E, it is also found that the HTA-derived perovskite film is destroyed. The LTA-derived perovskite film shows few random-oriented small crystalline grains, as shown in Figure 2F. In RCA strategy, the high temperature step is beneficial to obtain the continuous large grains and the low-temperature annealing step further promotes the formation of the high-quality perovskite films. In addition, the thickness of the HTA- and LTA-derived perovskite films is similar to that of the RCA-derived perovskite film. AFM images were applied to analyze the roughness of perovskite films. From Figure 2G–I, the root-mean-square (RMS) values of perovskite films based on RCA, HTA, and LTA are 23.1, 47.2, and 32.8 nm, respectively. The results indicate that the RCA strategy effectively promotes the formation of ideal perovskite films.

The crystallinity of perovskite films is confirmed by X-ray diffraction (XRD) measurement, as shown in Figure 3A. The diffraction peak at 14.2 ° of (111) plane for the RCA-based perovskite film has a higher intensity than those of the HTA- and LTA-based perovskite films.[11] The diffraction peaks at around 28 ° are observed for all perovskite films, which can be assigned to the (202) plane.[11] Furthermore, the peaks at around 28 ° can be split, due to the (004) plane of 3D-like perovskite phase.[28] Especially, the HTA-based perovskite film shows the visible diffraction peak of PbI_2 at 12.6 °, as shown in Figure 3B.[29] The exposed PbI_2 comes from the dissociation of perovskite films, which is consistent with the SEM image (Figure 2B). The results indicate that the RCA strategy promotes crystal growth of perovskite films. Meanwhile, RCA- and LTA-based perovskite films show a diffraction peak at 15.5 °, which can be assigned as the (100) planes of $MAPbCl_3$ crystals.[30] The related reports demonstrate that $MAPbCl_3$ clusters are formed from MACl and $PbCl_2$, which is beneficial for obtaining a compact and pinhole-free perovskite film.[31]

Figure 3C shows the absorption spectra of perovskite films based on LTA, HTA, and RCA. It is found that the absorption peaks at about 560, 607, 644, and 754 nm are

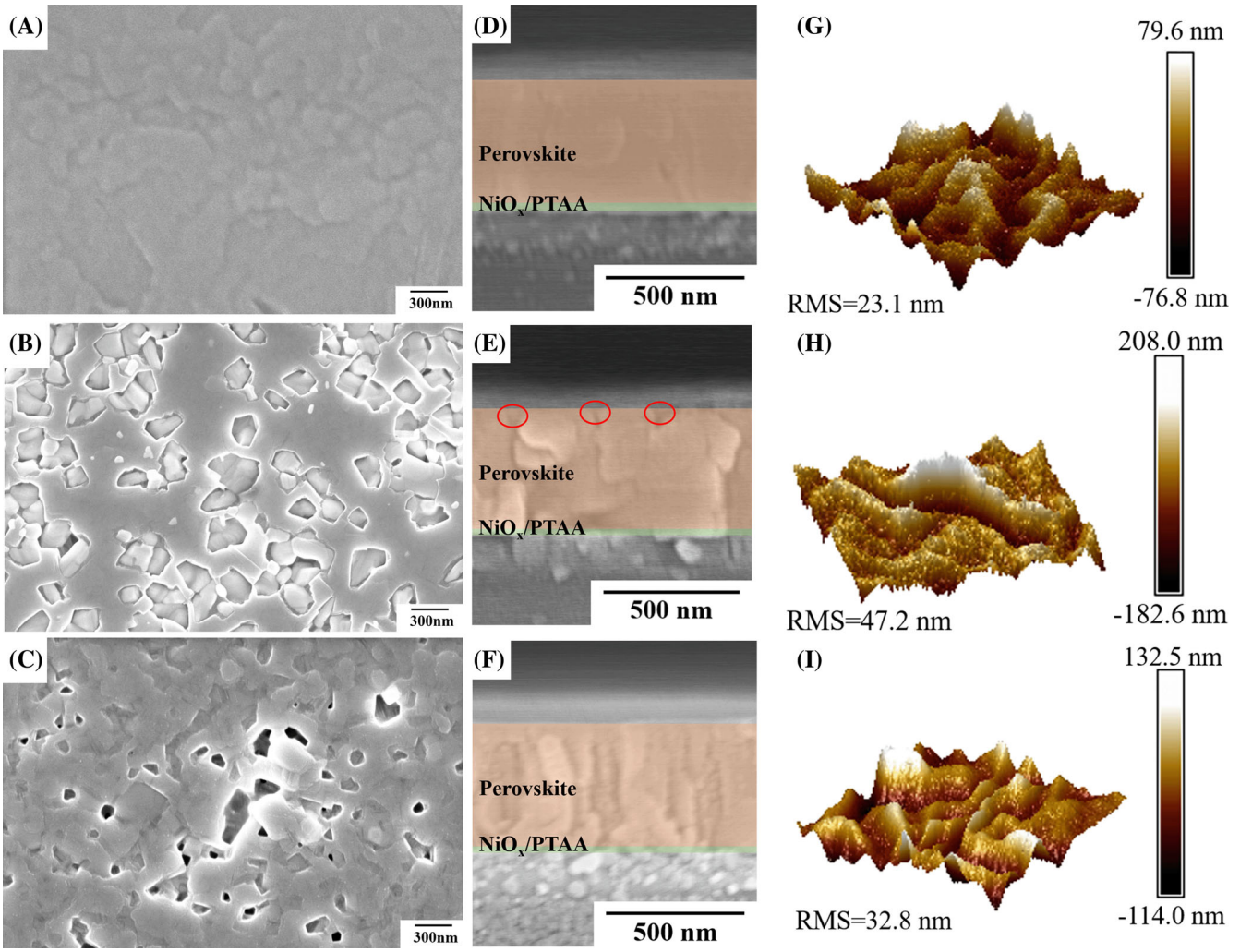

FIGURE 2 Plane-view and cross-sectional SEM images of perovskite films based on RCA (A, D), HTA (B, E), and LTA (C, F). AFM images of perovskite films based on RCA (G), HTA (H), and LTA (I).

observed, which can be assigned to low-n phases ($n = 2$, 3, 4) and 3D-like phases of HTA-based perovskite film, respectively.[11,32,33] For RCA- and LTA-based perovskite films, the excitonic absorption peaks of $n = 2$, 3, and 4 phases are blue-shifted to 539, 586, and 626 nm, respectively.[31] Meanwhile, the excitonic absorption peak of 3D-like phases is also blue-shifted from 754 to 742 nm. Figure S4 shows the Tauc plots of perovskite films. It is found that the bandgap of RCA- and LTA-based perovskite films is slightly larger than that of HTA-based perovskite film.[31] The defect and charge dynamics of perovskite films are investigated by steady-state PL and time-resolved photoluminescence (TRPL). Figure 3D shows the PL spectra of perovskite films excited from glass side. The PL emission peaks located from 553 to 561 nm, corresponding to the low-n phases with $n = 2$ for perovskite films. It is necessary to note that the LTA-based perovskite film exhibits a low degree of vertical orientation by using 4FPEA as bulky large cation.[8] The RCA- and HTA-based perovskite films not only have stronger PL emission peaks from the low-n phases with $n = 2$, but also display emission peaks from the low-n phases ($n = 3$ and 4). Furthermore, the RCA-based perovskite film exhibits highest PL intensity from 3D-like phases than those of the HTA- and LTA-based perovskite films, indicating the low defect density. Therefore, the degree of vertical orientation has been greatly improved for the RCA-based perovskite film.[11] Figure 3E shows PL spectra of perovskite films excited from film side. There are only emission peaks of 3D-like phases. Compared the HTA-based perovskite film, the emission peak is blue-shifted from 769 to 761 nm for the LTA- and RCA- based perovskite films. The results from absorption and PL spectra agree very well with each other. From Figure 3D, E, it is implied that the perovskites with the low-n phases grow from the substrates, while the perovskites 3D-like phases form from the surface. Figure 3F shows the TRPL spectra of perovskite films to analyze their charge

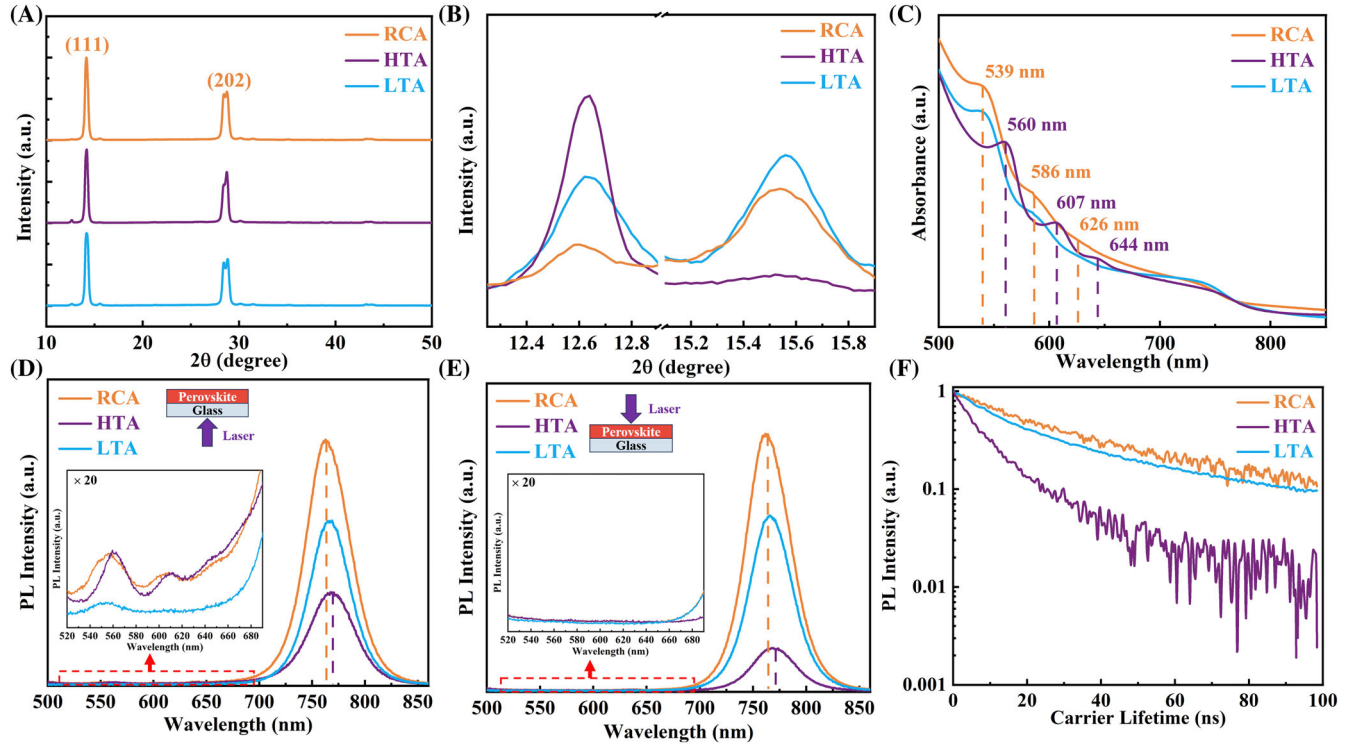

FIGURE 3 XRD patterns (A), the enlarged diffraction peak of PbI_2 and $MAPbCl_3$ (B), absorption spectra (C), PL spectra with a 447 nm continuous-wave laser as excitation source from glass side (D) and film side (E), and TRPL spectra (F) of perovskite films.

Film	d (nm)	τ_{PVK} (ns)	τ_{PCBM} (ns)	τ_{HTL} (ns)	$L_{D,e}$ (nm)	$L_{D,h}$ (nm)
RCA	440	56.3	33.4	21.4	232.1	357.9
HTA	440	10.1	9.0	8.1	98.0	139.3
LTA	440	30.4	19.4	22.7	211.0	163.2

TABLE 1 Carrier diffusion lengths of the RCA-, HTA-, and LTA-based perovskite films.

lifetime. A bi-exponential decay function is applied to fit TRPL spectra.[34–37] Generally, the fast decay process (τ_1) corresponds to the non-radiative recombination. The slow decay component (τ_2) corresponds to the bimolecular recombination of free charge carriers. The τ_1 values of the RCA-, HTA-, and LTA-based perovskite films are 22.2, 4.3, and 8.1 ns, respectively. The corresponding τ_2 values are 192.5, 17.2, and 45.2 ns, respectively. The calculated average charge lifetimes ($\tau_{average}$) of the RCA-, HTA-, and LTA-based perovskite films are 56.3, 10.1, and 30.4 ns, respectively. The long $\tau_{average}$ values indicate that the charge transport ability of the RCA-based perovskite film is effectively enhanced by reducing defects. Meanwhile, the charge carrier diffusion length (L_D) of perovskite films is calculated with the following equation (1).[38]

$$L_D \approx \frac{2d}{\pi}\sqrt{\frac{\tau_{average}}{\tau_{quench}} - 1} \quad (1)$$

where d is the thickness of perovskite films. $\tau_{average}$ and τ_{quench} are the average charge lifetimes without and with carrier transport layers, respectively. Figure S5 shows TRPL spectra of the composite films with the structure of ITO/perovskite/PCBM and ITO/NiO_x/PTAA/perovskite. The τ_{quench} values of perovskite films are calculated and summarized in Table 1. Carrier diffusion lengths are also calculated by the equation (1). From Table 1, the RCA-based perovskite film shows the longest electron diffusion length (232.1 nm) and hole diffusion length (357.9 nm), demonstrating the high-quality of the RCA-based perovskite film. Especially, the hole diffusion length has been greatly enhanced, due to the improved degree of vertical orientation for the RCA-based perovskite film.

An intrinsic formation mechanism of high-quality perovskite films is further investigated by grazing-incidence wide-angle X-ray scattering (GIWAXS). Figure S6a, b shows GIWAXS patterns of perovskite films based on LTA and RCA. Bragg spots with high intensity are observed in perovskite films, indicating the vertical crystal orientation.[32,39,40] The main reason is that the 4FPEA bulky large cation facilitates perovskite crystals preferentially growing along the out-of-plane direction. However,

the weakly Debye–Scherrer ring of the (111) plane in the perovskite film based on LTA is also observed. It demonstrates that the low degree of vertical orientation for LTA-based perovskite film is shown in Figure S6d.[39] For the RCA strategy, the perovskite film exhibits slightly sharper and narrower Bragg spots than those of the LTA-based perovskite film. Meanwhile, the line-cut profile curves of the (111) plane are extracted and shown in Figure S6c. The peak intensity of the (111) plane along the out-of-plane direction ($q_z = 1$ Å^{-1}) of the RCA-based perovskite film is larger than that of the LTA-based perovskite film. The results from Figure S6a-c show that the degree of vertical orientation has been effectively increased for RCA-based perovskite film (shown in Figure S6e). Therefore, it demonstrates that the charge transport and extraction of perovskite films are improved by the RCA strategy, which are in good agreement with PL and TRPL spectra.

The inverted PSCs with an architecture of ITO/NiO_x/PTAA/$(4FPEA)_2(MA_{0.9}FA_{0.1})_3Pb_4I_{13}$/PCBM/BCP/Ag are fabricated. The photovoltaic performance of PSCs based on RCA, HTA, and LTA is firstly investigated by *J-V* curves, as shown in Figure 4A. Generally, photovoltaic parameters include J_{sc}, open-circuit voltage (V_{oc}), fill factor (FF), and PCE. It is found that the champion PCE of the RCA-based PSC is up to 17.8% with a V_{oc} of 1.21 V, a J_{sc} of 19.19 mA cm^{-2}, and a FF of 76.45%. The V_{oc}, J_{sc}, FF, and PCE of the LTA-based PSC are 1.17 V, 14.92 mA cm^{-2}, 72.81%, and 12.7%, respectively. The HTA-based PSC shows a low PCE of 7.8% ($V_{oc} = 1.18$ V, $J_{sc} = 13.85$ mA cm^{-2}, and FF = 47.91%). The main reason for the increase in FF is the improved crystal quality of the RCA-based perovskite film.[41] The V_{oc} value achieves 1.21 V, which can be attributed to the small non-radiative V_{oc} loss. Importantly, the RCA-based PSC exhibits the highest J_{sc} value, due to the high-quality perovskite film grown along the out-of-plane direction. From Figure S7, the RCA- and LTA-based PSCs exhibit the less hysteresis index. Furthermore, the J_{sc} value can be proved by EQE spectra, as shown in Figure 4B. The integrated current densities of PSCs based on RCA, HTA, and LTA are 18.36, 13.77, and 14.41 mA cm^{-2}, respectively.[42] The calculated J_{sc} values are consistent with the *J-V* curves. Figure 4C and Figure S8 show the statistical distribution of photovoltaic parameters of PSCs based on RCA, HTA, and LTA. The RCA-based PSC exhibits very well repeatability for 20 devices. Figure S9 shows the

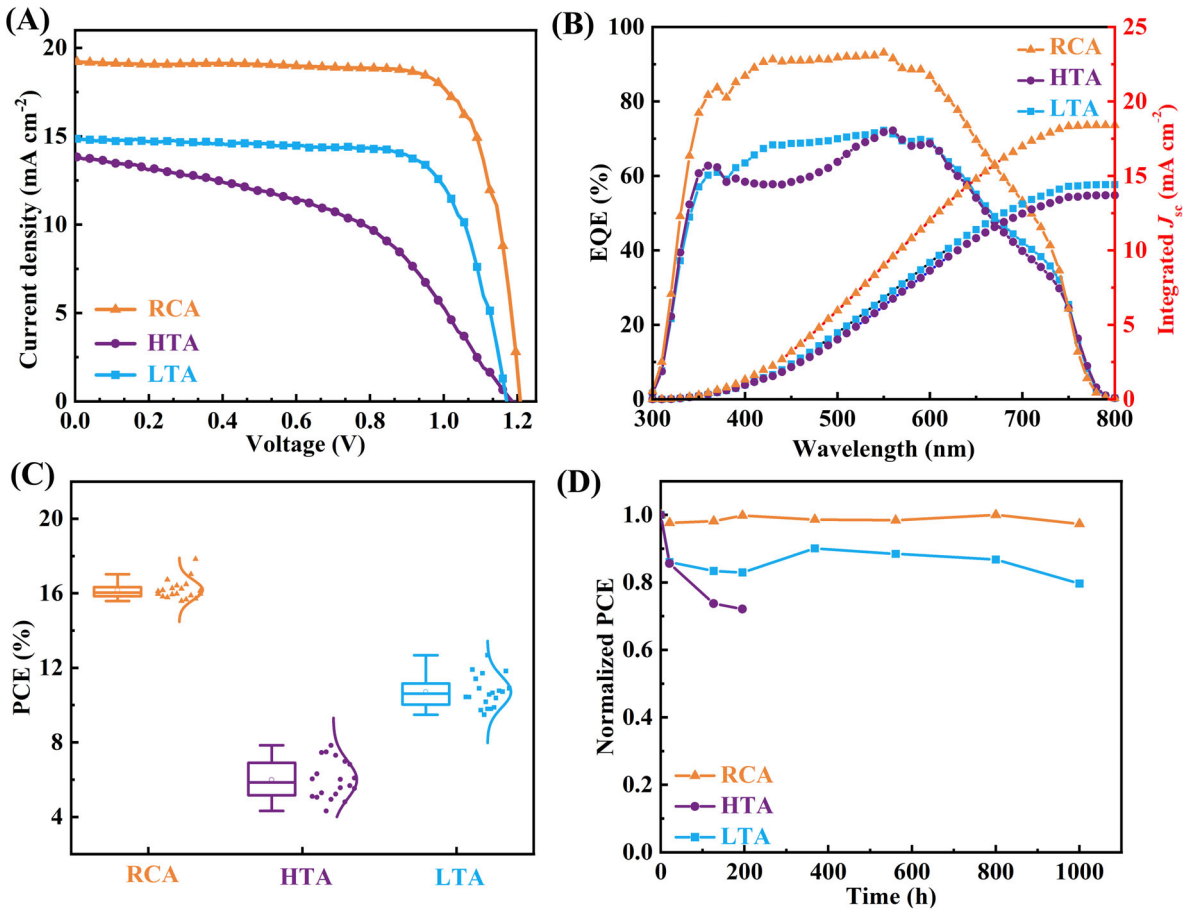

FIGURE 4 *J-V* curves (A), EQE spectra (B), and PCE statistics (C) of PSCs based on RCA, HTA, and LTA. (D) Normalized PCE evolution of PSCs without encapsulation stored in a nitrogen-filled glove box.

steady-state output of PSCs based on RCA, HTA, and LTA at a maximum power point for 200 s. The steady-state output for photocurrent density of PSCs based on RCA, HTA, and LTA are 17.87, 9.56, and 13.61 mA cm^{-2}, respectively. The corresponding stable PCEs are 17.7% (V_{max} at 0.99 V), 7.7% (V_{max} at 0.81 V), and 12.9% (V_{max} at 0.95 V), respectively. The RCA-based PSC displays good illumination stability. Then, the long-term stability of PSCs without encapsulation stored in a nitrogen-filled glove box is shown in Figure 4D. The HTA-based PSC remains only 72.1% of its original PCE after 195 h. Meanwhile, the PCE of the LTA-based PSC remains 79.7% of its original PCE after 1000 h. Especially, the RCA-based PSC has excellent long-term stability and remains 97.4% of the initial PCE after 1000 h.

The reason of the increase in photovoltaic performance is explored in detail. The trap density of hole-only devices with ITO/NiO_x/PTAA/$(4FPEA)_2(MA_{0.9}FA_{0.1})_3Pb_4I_{13}$/Spiro-OMeTAD/Ag is studied by dark current–voltage curves through the space-charge-limited current (SCLC) method. Figure S10 shows dark current–voltage curves of hole-only devices. Generally, a trap-filled limit voltage (V_{TFL}) is defined by the onset voltage of the trap-filled limit region. A higher trap-filled limit voltage (V_{TFL}) indicates a larger trap-state density.[43,44] The relationship of V_{TFL} and the trap-state density (n_t) can be described by Equation (2)[11]:

$$V_{TFL} = \frac{en_tL^2}{2\varepsilon_r\varepsilon_0} \quad (2)$$

where ε_0 is the vacuum dielectric constant, ε_r is the relative dielectric constant of perovskite films, e is the elemental charge, and L is the thickness of the perovskite films. The V_{TFL} values of hole-only devices based on RCA, HTA, and LTA are 0.68, 2.18, and 0.82 V, respectively. The calculated trap-state densities of the perovskite films based on RCA, HTA, and LTA are 9.7×10^{15} cm^{-3}, 3.1×10^{16} cm^{-3}, and 1.2×10^{16} cm^{-3}, respectively. It can be seen that the RCA-based perovskite film has the smallest trap-state density, resulting from the high-quality perovskite film. The charge transport kinetics of perovskite films are further studied by preparing PSCs. Figure 5A shows dark current–voltage curves of PSCs based on RCA, HTA, and LTA. The reverse-bias saturation current (I_0) of the RCA-, HTA-, and LTA-based PSCs are 4.9×10^{-4} mA, 1.3×10^{-1} mA, and 3.6×10^{-2} mA, respectively. The lower I_0 value indicates that the RCA-based PSC exhibits the lower defect density and charge recombination.[45,46] Figure 5B shows Mott-Schottky (*M-S*) plots of PSCs based on RCA, HTA, and LTA. The built-in potential (V_{bi}) values of the RCA-, HTA-, and LTA-based PSCs are 1.16, 0.99, and 1.13 V, respectively. The enhancement of V_{bi} value for the RCA-based PSC implies the enhanced driving force to separate photogenerated charge carriers and the extended

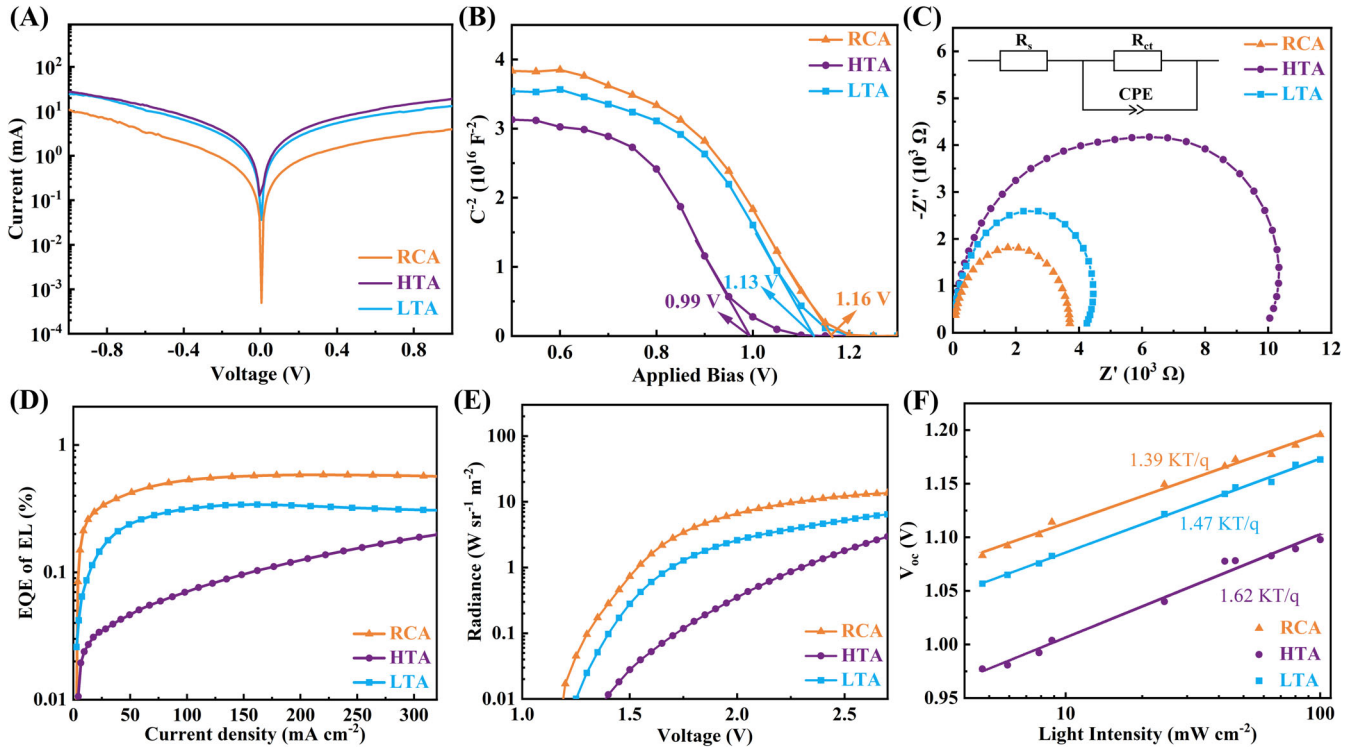

FIGURE 5 Dark current–voltage curves (A), Mott-Schottky plots (B), the Nyquist plots (C), EQE of electroluminescence versus current density curves (D), radiance versus voltage curves (E), and V_{oc} versus light intensity (F) of PSCs. The inset of (C) is the equivalent circuit model.

depletion region to suppress electron–hole recombination, due to the continuous large grains of the perovskite film with RCA.[20,47,48] It is also suggested that the non-radiative recombination is suppressed by fabricating high-quality perovskite films, which is beneficial to reducing the non-radiative open-circuit voltage loss.

The charge transport ability is also discussed by Nyquist plots of electrochemical impedance spectra (EIS), as shown in Figure 5C. Nyquist plots of PSCs with RCA, HTA, and LTA are conducted under open-circuit voltage in dark conditions. At the high-frequency region, the semicircle represents the charge transfer resistance (R_{ct}) of PSCs.[49,50] Generally, the smaller R_{ct} value indicates the stronger charge transport ability. The R_{ct} value of the PSC with RCA is 3.65 kΩ, which smaller than those of the PSC with HTA (10.38 kΩ) and PSC with LTA (4.61 kΩ). Thus, the PSC with RCA shows the smallest R_{ct} value, demonstrating that the carrier transport and extraction becomes more efficient. Furthermore, the non-radiative open-circuit voltage (V_{oc}) loss of PSCs is investigated by the EQE of electroluminescence (EQE_{EL}) under the dark condition. Figure 5D shows EQE_{EL} spectra of PSCs. Generally, non-radiative V_{oc} loss is described as following.[51]

$$\Delta V_{oc}^{non\text{-}rad} = -\frac{KT}{q}\ln(EQE_{EL}) \quad (3)$$

where $\Delta V_{oc}^{non\text{-}rad}$ is V_{oc} loss by the non-radiative recombination. EQE_{EL} value is depended by setting the injection current density as J_{sc}. K is the Boltzmann constant. T is the Kelvin temperature. q is the elemental charge. From Figure 5D, the EQE_{EL} values of PSCs with RCA, HTA, and LTA are 0.306%, 0.028%, and 0.107%, respectively. The corresponding $\Delta V_{oc}^{non\text{-}rad}$ values are 149, 210, and 176 mV, respectively. From Figure 5E, the radiance of the RCA-based PSC is larger than those of the HTA- and LTA-based PSCs, indicating the low non-radiative recombination. Thus, the RCA-based PSC displays the lowest energy loss, which is agreement with the results from Mott-Schottky plots (Figure 5B). Figure 5F shows V_{oc} versus light intensity curves of PSCs. The slope is expressed as following: nKT/q.[52,53] Where n is the diode ideality factor. The larger n value suggests the increase of monomolecular Shockley-Read-Hall (SRH) recombination process. The n values of PSCs with RCA, HTA, and LTA are 1.39, 1.62, and 1.47, respectively. The SRH recombination is suppressed for the RCA-based PSC.

3 | CONCLUSION

In conclusion, our study has successfully demonstrated the reverse-cool annealing strategy for the fabrication of high-quality 2D RP perovskite films with preferred growth along the out-of-plane direction. These 2D RP perovskite films exhibit a compact and pinhole-free morphology, which significantly reduces defects and enhances charge transport capabilities. Consequently, 2D RP PSCs display a high charge carrier extraction efficiency and a minimal non-radiative open-circuit voltage loss (149 mV). The leading 2D RP PSC in our research achieved an outstanding PCE of 17.8%. Furthermore, the long-term stability of these PSCs, even when stored in a nitrogen environment for over 1000 h, showed no significant deterioration. Our work introduces a promising annealing strategy to produce high-performance 2D RP perovskite films, paving the way for the advancement of 2D PSCs in practical applications.

4 | METHODS

4.1 | Materials

Polymer polybis(*4*-phenyl)(*2,4,6*-trimethylphenyl)amine (PTAA, molecular weight: 1000–10 000 g mol^{-1}), 4-fluorophenylethylammonium iodide (4FPEAI, 99%), lead (II) iodide (PbI_2, 99.9%), methylammonium chloride (MACl, 99.5%), formamidinium iodide (FAI, 99.5%), methylammonium iodide (MAI, 99.9%), lead(II) chloride ($PbCl_2$, 99.9%), *2,9*-dimethyl-*4,7*-diphenyl-*1,10*-phenanthroline (BCP, 99%), 6,6-phenyl C61 butyric acid methyl ester (PCBM, 99%), *2,2′,7,7′*-tetrakisN, N-di(4-methoxyphenyl)amino-*9,9′*-spirobifluorene (Spiro-OMeTAD, ≥99.5%), *4*-tert-Butylpyridine (TBP, >96%), and lithium bis(trifluoromethanesulphonyl)imide (LiTFSI, >99%) were purchased from Xi'an polymer light technology Corp. N, N-dimethylformamide (DMF, 99.8%), dimethyl sulfoxide (DMSO, 99.9%), chlorobenzene (CB, 99.8%), Isopropyl alcohol (IPA, 99.8%), and acetonitrile (99.9%) were purchased from Sigma-Aldrich. Ammonium hydroxide (NH_4OH, 25.0%–28.0%) purchased from Sinopharm Chemical Reagent Co., Ltd. Acetylacetone ($C_5H_8O_2$, 99%) and 2-methoxyethanol ($C_3H_8O_2$, 99.3%) were purchased from Alfa Aesar. Nickel (II) nitrate hexahydrate ($Ni(NO_3)_2{\cdot}6H_2O$, 98%) was purchased from Shanghai Aladdin Biochemical Technology Co., Ltd. All the materials were used directly without further purification.

4.2 | Preparation of precursor solutions

NiO_x precursor solution was prepared by dissolving 290.79 mg of $Ni(NO_3)_2{\cdot}6H_2O$ in 10 mL of 2-methoxyethanol and then adding 100 μL of ammonium hydroxide and 100 μL of acetylacetone, respectively. PTAA solution with 2 mg mL^{-1} was obtained by dissolving PTAA in CB at

room temperature. 2D RP perovskite $(4FPEA)_2(MA_{0.9}FA_{0.1})_3Pb_4I_{13}$ ($n = 4$) precursor solution with 1.1 M was prepared by dissolving 14.2 mg of FAI, 118.0 mg of MAI, 507.1 mg of PbI_2, 7.5 mg of MACl, 30.6 mg of $PbCl_2$, and 147.1 mg of 4FPEAI in a solution including 50 μL of DMSO and 950 μL of DMF. PCBM solution with 20 mg mL^{-1} was obtained by dissolving PCBM in CB at room temperature. BCP solution with 0.5 mg mL^{-1} was obtained by dissolving BCP in IPA at room temperature. Spiro-OMeTAD precursor solution was prepared by dissolving 56.4 mg of Spiro-OMeTAD, 22.6 μL of TBP, and 14.04 μL of LiTFSI (520 mg mL^{-1} in acetonitrile) into 780 μL of CB.

4.3 | Device fabrication

The cleaned indium tin oxide (ITO) glasses were treated with ultraviolet-ozone for 15 min. NiO_x films were synthesized by spin-coating NiO_x precursor solution on ITO glasses at 4000 rpm for 30 s and heating at 250 °C for 40 min. Then, NiO_x films were transferred into the glove box with nitrogen. NiO_x/PTAA films were obtained by spin-coating PTAA solution on NiO_x films at 5000 rpm for 60 s and heating at 100 °C for 10 min. 2D RP perovskite $(4FPEA)_2(MA_{0.9}FA_{0.1})_3Pb_4I_{13}$ ($n = 4$) precursor solution was spin-coated on NiO_x/PTAA film at 5000 rpm for 15 s. After that, the wet film was sequentially annealed at 120 °C for 8 s and 80 °C for 5 min. The as-fabricated process of 2D RP perovskite films was defined as RCA. Meanwhile, 2D RP perovskite films were also fabricated by annealing at 120 °C for 5 min (HTA) or 80 °C for 5 min (LTA). In the following step, the PCBM solution was spin-coated on 2D RP perovskite films at 2500 rpm for 60 s and heated at 80 °C for 10 min. BCP solution was also spin-coated at 3500 rpm for 30 s and heated at 80 °C for 10 min. At last, a thermal evaporation system was used to prepare an Ag electrode with 70 nm.

4.4 | Measurement and characterization

The scanning electron microscope (SEM, Quanta 250 FEG) and atom force microscope (AFM, Bruker Dimension Icon) was used to character the morphology and roughness of 2D RP perovskite films. The X-ray diffraction (XRD, D8 DISCOVER) and grazing-incidence wide-angle X-ray scattering (GIWAXS, Xeuss 2.0 SAXS/WAXS system) were used to analyze the phases and crystal direction of 2D RP perovskite films. Cu X-ray source (8.05 keV, 1.54 Å) and a Pilatus3R 300 K detector were used for the GIWAXS measurement. The incident angle was set as 1 °. In photoluminescence (PL) system, a continuous-wave solid state laser with wavelength of 447 nm was used as the excitation pump. The signal was collected by an optical fiber coupled CCD spectrometer. For the time-resolved PL (TRPL) measurements, the expectation was use a Q-switched Nd:YAG pulsed laser (532 nm, the pulse duration is about 350 ps with repetition rate of 50 Hz) for excitation intensity of 1 μJ cm^{-2}. The PL signal was detected by 1 GHz Si amplified photodetector, which was connected to a 1 GHz digital oscilloscope. The UV–vis–NIR spectrophotometer (UV-3600, Shimadzu) was used to characterize the absorption spectra of 2D RP perovskite films. The in situ absorption test system comprises a xenon lamp (7ILX150, Beijing 7-Star Optical Instruments Co., Ltd.) and a spectrometer (PG2000-Pro, Shanghai Ideaoptics Corp., Ltd). The dark current–voltage curves, electrochemical impedance spectra (EIS), and Mott-Schottky (*M-S*) curves of 2D RP PSCs were characterized by CHI660E electrochemical workstation. Trap state density and charge mobility of the symmetrical devices were analyzed by the space-charge-limited current (SCLC). The structure of the symmetrical devices was ITO/NiO_x/PTAA/$(4FPEA)_2(MA_{0.9}FA_{0.1})_3Pb_4I_{13}$/Spiro-OMeTAD/Ag. The external quantum efficiency (EQE) of 2D RP PSCs was measured by the QE-R system (EnliTechnology Co., Ltd.). The luminance and electroluminescence (EL) spectra of 2D RP PSCs was measured by a luminance meter (Konica Minolta, CS-200) and Flame spectrometer (Ocean Optic), respectively. The PCE of 2D RP PSCs was calculated through current density-voltage (*J-V*) curves, which were obtained by Keithley 2450 source meter under standard sunlight (AM 1.5 G, 100 mW cm^{-2}). The standard sunlight was obtained from the solar simulator (CHF-XM-500 W, Beijing perfectlight Technology Co., Ltd.) and calibrated by irradiance meter (FZ-A). The unencapsulated 2D RP PSCs were stored in a nitrogen atmosphere under dark conditions for long-term stability measurement.

AUTHOR CONTRIBUTIONS

Zhongqi Xie: Investigation, Writing – original draft. **Qing-Song Jiang**: Supervision, Writing – review & editing. **Ya Zhao**: Validation. **Ligang Yuan**: Data curation. **Keyou Yan**: Methodology. **Yong Peng**, **Huiming Luo**, **Mojtaba Abdi-Jalebi**: Supervision, Writing – review & editing.

ACKNOWLEDGMENTS

This work was financially supported by National Natural Science Foundation of China (No. 61804062), the open research fund of State Key Laboratory of Advanced Technology for Materials Synthesis and Processing (Wuhan University of Technology) (No. 2023-KF-21), and the open research fund of State Key Laboratory of Organic

Electronics and Information Displays (No. SKL2023004). The authors thank support from The Chinese University of Hong Kong for GIWAXS. M. Abdi-Jalebi acknowledges Cambridge Materials Limited for its funding and technical support. M. Abdi-Jalebi acknowledges the Department for Energy Security and Net Zero (Project ID: NEXTCCUS), University College London's Research, Innovation and Global Engagement, Cornell-UCL Global Strategic Collaboration Awards, and University of Sydney-University College London Partnership Collaboration Awards for their financial support. M. Abdi-Jalebi acknowledges the ACT program (Accelerating CCS Technologies, Horizon2020 Project No. 691712) for the financial support of the NEXTCCUS project (project ID: 327327). M. Abdi-Jalebi wishes to acknowledge the support of the Henry Royce Institute for Advanced Materials through the Industrial Collaboration Programme and MATcelerateZero, funded from a grant provided by the Engineering and Physical Sciences Research Council EP/X527257/1. This work was supported by the Henry Royce Institute for advanced materials through the Equipment Access Scheme enabling access to the Royce SEM-FIB Suite at Cambridge; Cambridge Royce facilities grant EP/P024947/1 and Sir Henry Royce Institute - recurrent grant EP/R00661X/1. H. Luo is grateful for the support from the Chinese Scholarship Council (CSC) and the Faculty of Mathematical & Physical Sciences (MAPS) at University College London (UCL).

CONFLICT OF INTEREST STATEMENT

Huaiyin Institute of Technology of China has submitted patent applications related to the subject to Chinese National Intellectual Property Administration on 16 Dec. 2022 (CN 202211621354.9), the authors are part of inventors.

ORCID

Mojtaba Abdi-Jalebi https://orcid.org/0000-0002-9430-6371

REFERENCES

1. Zhang T, Wang F, Kim H-B, et al. Ion-modulated radical doping of spiro-OMeTAD for more efficient and stable perovskite solar cells. *Science*. 2022;377(6605):495-501. doi:10.1126/science.abo2757
2. Ma C, Eickemeyer FT, Lee S-H, et al. Unveiling facet-dependent degradation and facet engineering for stable perovskite solar cells. *Science*. 2023;379(6628):173-178. doi:10.1126/science.adf3349
3. NREL. NREL efficiency chart. https://www.nrel.gov/pv/cell-efficiency.html
4. Park J, Kim J, Yun H-S, et al. Controlled growth of perovskite layers with volatile alkylammonium chlorides. *Nature*. 2023;616(7958):724-730. doi:10.1038/s41586-023-05825-y
5. Zhao Y, Ma F, Qu Z, et al. Inactive $(PbI_2)_2RbCl$ stabilizes perovskite films for efficient solar cells. *Science*. 2022;377(6605):531-534. doi:10.1126/science.abp8873
6. Park SM, Wei M, Xu J, et al. Engineering ligand reactivity enables high-temperature operation of stable perovskite solar cells. *Science*. 2023;381(6654):209-215. doi:10.1126/science.adi4107
7. Li C, Wang X, Bi E, et al. Rational design of Lewis base molecules for stable and efficient inverted perovskite solar cells. *Science*. 2023;379(6633):690-694. doi:10.1126/science.ade3970
8. Shi J, Gao Y, Gao X, et al. Fluorinated low-dimensional Ruddlesden-popper perovskite solar cells with over 17% power conversion efficiency and improved stability. *Adv Mater*. 2019;31(37):1901673. doi:10.1002/adma.201901673
9. Fu W, Liu H, Shi X, et al. Tailoring the functionality of organic spacer cations for efficient and stable quasi-2D perovskite solar cells. *Adv Funct Mater*. 2019;29(25):1900221. doi:10.1002/adfm.201900221
10. Liang J, Zhang Z, Xue Q, et al. A finely regulated quantum well structure in quasi-2D Ruddlesden-popper perovskite solar cells with efficiency exceeding 20%. *Energ Environ Sci*. 2022;15(1):296-310. doi:10.1039/D1EE01695D
11. Shao M, Bie T, Yang L, et al. Over 21% efficiency stable 2D perovskite solar cells. *Adv Mater*. 2022;34(1):2107211. doi:10.1002/adma.202107211
12. Gao L, Zhang F, Xiao C, et al. Improving charge transport via intermediate-controlled crystal growth in 2D perovskite solar cells. *Adv Funct Mater*. 2019;29(47):1901652. doi:10.1002/adfm.201901652
13. He T, Li S, Jiang Y, et al. Reduced-dimensional perovskite photovoltaics with homogeneous energy landscape. *Nat Commun*. 2020;11(1):1672. doi:10.1038/s41467-020-15451-1
14. Yang Y, Liu C, Syzgantseva OA, et al. Defect suppression in oriented 2D perovskite solar cells with efficiency over 18% viarerouting crystallization pathway. *Adv Energy Mater*. 2021;11(1):2002966. doi:10.1002/aenm.202002966
15. Yang R, Li R, Cao Y, et al. Oriented quasi-2D perovskites for high performance optoelectronic devices. *Adv Mater*. 2018;30(51):1804771. doi:10.1002/adma.201804771
16. Xu Z, Lu D, Liu F, et al. Phase distribution and carrier dynamics in multiple-ring aromatic spacer-based two-dimensional Ruddlesden-popper perovskite solar cells. *ACS Nano*. 2020;14(4):4871-4881. doi:10.1021/acsnano.0c00875
17. Yu S, Yan Y, Chen Y, et al. Enabling room-temperature processed highly efficient and stable 2D Ruddlesden-popper perovskite solar cells with eliminated hysteresis by synergistic exploitation of additives and solvents. *J Mater Chem A*. 2019;7(5):2015-2021. doi:10.1039/C8TA09146C
18. Zhang X, Wu G, Yang S, et al. Vertically oriented 2D layered perovskite solar cells with enhanced efficiency and good stability. *Small*. 2017;13(33):1700611. doi:10.1002/smll.201700611
19. Chao L, Wang Z, Xia Y, et al. Recent progress on low dimensional perovskite solar cells. *J Energy Chem*. 2018;27(4):1091-1100. doi:10.1016/j.jechem.2017.10.013
20. Tsai H, Nie W, Blancon J-C, et al. High-efficiency two-dimensional Ruddlesden-popper perovskite solar cells. *Nature*. 2016;536(7616):312-316. doi:10.1038/nature18306
21. Zhang X, Yang T, Ren X, et al. Film formation control for high performance Dion-Jacobson 2D perovskite solar cells. *Adv Energy Mater*. 2021;11(19):2002733. doi:10.1002/aenm.202002733

22. Lin Y, Fang Y, Zhao J, et al. Unveiling the operation mechanism of layered perovskite solar cells. *Nat Commun*. 2019;10(1):1008. doi:10.1038/s41467-019-08958-9
23. Wang C, Zhao Y, Ma T, et al. A universal close-space annealing strategy towards high-quality perovskite absorbers enabling efficient all-perovskite tandem solar cells. *Nat Energy*. 2022;7(8):744-753. doi:10.1038/s41560-022-01076-9
24. Chang X, Zhong J-X, Li S, et al. Two-second-annealed 2D/3D perovskite films with graded energy funnels and toughened heterointerfaces for efficient and durable solar cells. *Angew Chem Int Ed*. 2023;62(38):e202309292. doi:10.1002/anie.202309292
25. Liu Y-C, Lin J-T, Lee Y-L, et al. Recognizing the importance of fast nonisothermal crystallization for high-performance two-dimensional Dion-Jacobson perovskite solar cells with high fill factors: a comprehensive mechanistic study. *J Am Chem Soc*. 2022;144(32):14897-14906. doi:10.1021/jacs.2c06342
26. Kang Y, Wang A, Li R, et al. Thermal shock fabrication of ion-stabilized perovskite and solar cells. *Adv Mater*. 2022;34(32):2203166. doi:10.1002/adma.202203166
27. Zhang X, Ye J, Zhu L, et al. High-efficiency perovskite solar cells prepared by using a sandwich structure MAI-PbI_2-MAI precursor film. *Nanoscale*. 2017;9(14):4691-4699. doi:10.1039/C6NR07689K
28. Zhang X, Einhaus L, Hu A et al. Manipulation of crystal orientation and phase distribution of quasi-2D perovskite through synergistic effect of additive doping and spacer engineering. *Inorg Chem*. 2024;63(11):5246-5259. doi:10.1021/acs.inorgchem.4c00335
29. Wang H, Wang Z, Yang Z, et al. Ligand-modulated excess PbI_2 nanosheets for highly efficient and stable perovskite solar cells. *Adv Mater*. 2020;32(21):2000865. doi:10.1002/adma.202000865
30. Liu Y, Yang Z, Cui D, et al. Two-inch-sized perovskite $CH_3NH_3PbX_3$ (X = Cl, Br, I) crystals: growth and characterization. *Adv Mater*. 2015;27(35):5176-5183. doi:10.1002/adma.201502597
31. Wang Z, Liu L, Liu X, et al. Uncovering synergistic effect of chloride additives for efficient quasi-2D perovskite solar cells. *Chem Eng J*. 2022;432:134367. doi:10.1016/j.cej.2021.134367
32. Qing J, Liu X-K, Li M, et al. Aligned and graded type-II Ruddlesden-Popper perovskite films for efficient solar cells. *Adv Energy Mater*. 2018;8(21):1800185. doi:10.1002/aenm.201800185
33. Smith IC, Hoke ET, Solis-Ibarra D, et al. MD. A layered hybrid perovskite solar-cell absorber with enhanced moisture stability. *Angew Chem Int Ed*. 2014;53(42):11232-11235. doi:10.1002/anie.201406466
34. Seo H-K, Kim H, Lee J, et al. Efficient flexible organic/inorganic hybrid perovskite light-emitting diodes based on graphene anode. *Adv Mater*. 2017;29(12):1605587. doi:10.1002/adma.201605587
35. Zhu C, Wang X, Li H, et al. Stress compensation based on interfacial nanostructures for stable perovskite solar cells. *Interdiscip Mater*. 2023;2(2):348-359. doi:10.1002/idm2.12079
36. Xu J, Chen J, Chen S, et al. Organic spacer engineering of Ruddlesden-popper perovskite materials toward efficient and stable solar cells. *Chem Eng J*. 2023;453:139790. doi:10.1016/j.cej.2022.139790
37. Kong W, Zeng F, Su Z, et al. Oriented low-n Ruddlesden-popper formamidinium-based perovskite for efficient and air stable solar cells. *Adv Energy Mater*. 2022;12(46):2202704. doi:10.1002/aenm.202202704
38. Zhang Y, Chen M, He T, et al. Highly efficient and stable FA-based quasi-2D Ruddlesden-popper perovskite solar cells by the incorporation of β-Fluorophenylethanamine cations. *Adv Mater*. 2023;35(17):2210836. doi:10.1002/adma.202210836
39. Liang D, Dong C, Cai L, et al. Unveiling crystal orientation in quasi-2D perovskite films by in situ GIWAXS for high-performance photovoltaics. *Small*. 2021;17(33):2100972. doi:10.1002/smll.202100972
40. Liang J, Zhang Z, Zheng Y, et al. Overcoming the carrier transport limitation in Ruddlesden-popper perovskite films by using lamellar nickel oxide substrates. *J Mater Chem A*. 2021;9(19):11741-11752. doi:10.1039/D1TA01038G
41. Liang C, Gu H, Xia Y, et al. Two-dimensional Ruddlesden-popper layered perovskite solar cells based on phase-pure thin films. *Nat Energy*. 2021;6(1):38-45. doi:10.1038/s41560-020-00721-5
42. Xie Y-M, Yao Q, Xue Q, et al. Subtle side chain modification of triphenylamine-based polymer hole-transport layer materials produces efficient and stable inverted perovskite solar cells. *Interdiscip Mater*. 2022;1(2):281-293. doi:10.1002/idm2.12023
43. Tian W, Song P, Zhao Y, et al. Monolithic bilayered In_2O_3 as an efficient interfacial material for high-performance perovskite solar cells. *Interdiscip Mater*. 2022;1(4):526-536. doi:10.1002/idm2.12047
44. Wang H, Huang Z, Xiao S, et al. An in situ bifacial passivation strategy for flexible perovskite solar module with mechanical robustness by roll-to-roll fabrication. *J Mater Chem A*. 2021;9(9):5759-5768. doi:10.1039/D0TA12067G
45. SunLi Z, Liu Y, Li S, et al. 2D perovsktie substrate-assisted $CsPbI_3$ film growth for high-efficiency solar cells. *ACS Appl Mater Interfaces*. 2022;14(5):7417-7427. doi:10.1021/acsami.1c20968
46. Zheng L, Shen L, Zhu T, et al. Stable and efficient perovskite solar cells by discrete two-dimensional perovskites capped on the three-dimensional perovskites bilayer thin film. *Nano Energy*. 2022;96:107126. doi:10.1016/j.nanoen.2022.107126
47. Yang J, Xiong S, Song J, et al. Energetics and energy loss in 2D Ruddlesden-Popper perovskite solar cells. *Adv Energy Mater*. 2020;10(23):2000687. doi:10.1002/aenm.202000687
48. Li S, Liu J, Liu S, et al. Yttrium-doped Sn_3O_4 two-dimensional electron transport material for perovskite solar cells with efficiency over 23%. *EcoMat*. 2022;4(4):e12202. doi:10.1002/eom2.12202
49. Yuan L, Li J, Wang Z, et al. Diblock copolymer PF-b-PDMAEMA as effective cathode interfacial material in polymer solar cells. *ACS Appl Mater Interfaces*. 2017;9(49):42961-42968. doi:10.1021/acsami.7b11648
50. Huang J, Wang H, Li Y, Zhang F, et al. Diaminobenzene dihydroiodide-$MA_{0.6}FA_{0.4}PbI_{3-x}Cl_x$ unsymmetrical perovskites with over 22% efficiency for high stability solar cells. *Adv Funct Mater*. 2022;32(16):2110788. doi:10.1002/adfm.202110788
51. Yuan L, Wang J, Huang P, et al. Reexamining the post-treatment effects on perovskite solar cells: passivation and chloride redistribution. *Small Methods*. 2023;7(3):2201467. doi:10.1002/smtd.202201467
52. Xiao X, Zhang W, Liu J, et al. Depth-dependent post-treatment for reducing voltage loss in printable mesoscopic perovskite solar cells. *Adv Sci*. 2023;10(9):2206331. doi:10.1002/advs.202206331

53. Cao F, Zhu Z, Zhang C, et al. Synergistic ionic liquid in hole transport layers for highly stable and efficient perovskite solar cells. *Small*. 2023;19(27):2207784. doi:10.1002/smll.202207784

SUPPORTING INFORMATION

Additional supporting information can be found online in the Supporting Information section at the end of this article.

How to cite this article: Xie Z, Luo H, Jiang Q-S, et al. A universal reverse-cool annealing strategy makes two-dimensional Ruddlesden-popper perovskite solar cells stable and highly efficient with V_{oc} exceeding 1.2 V. *EcoMat*. 2024;e12501. doi:10.1002/eom2.12501